Applied Catalysis B: Environmental 117–118 (2012) 125–134

Contents lists available at SciVerse ScienceDirect

Applied Catalysis B: Environmental

journal homepage: www.elsevier.com/locate/apcatb

Catalytic oxidation of VOCs over mixed Co–Mn oxides

Zhen-Yu Tian*, Patrick Hervé Tchoua Ngamou[1], Vincent Vannier, Katharina Kohse-Höinghaus, Naoufal Bahlawane[2]

Department of Chemistry, Bielefeld University, D-33615 Bielefeld, Germany

ARTICLE INFO

Article history:
Received 22 November 2011
Received in revised form 3 January 2012
Accepted 9 January 2012
Available online 18 January 2012

Keywords:
Catalytic oxidation
Cobalt manganese oxide
Spinel
Pulsed-spray evaporation
Chemical vapor deposition

ABSTRACT

This work reports the synthesis and characterization of single-phase cobalt manganese oxide (CMO) spinels $Co_{3-x}Mn_xO_4$ ($0 \le x \le 0.34$) prepared by the pulsed-spray evaporation chemical vapor deposition (PSE–CVD) method. Structure and cationic distribution of the obtained films were characterized by XRD, FTIR, XPS and Raman spectroscopy. Temperature-programmed reduction/re-oxidation (TPR/TPO) was used to elucidate the redox properties of the deposited films. The electrical resistivity was measured in the temperature range of 27–450 °C. XRD, FTIR and Raman spectra reveal the formation of single-phase cubic spinel structures up to $x = 0.34$. With the substitution of cobalt cations with Mn^{3+} and Mn^{4+} ions, the unit cell of the cubic spinel shows a linear increase; the TPR results indicate a lower reducibility while the TPO results display no evident change; also, the ratio Co^{3+}/Co^{2+} decreased and both electrical resistivity and thermal stability showed increasing trends. The observed behavior is attributed to the progressive incorporation of manganese, which induces structural defects favoring the formation of anionic vacancies and the restriction of the oxygen mobility. The catalytic activities of the doped spinels were investigated for the deep oxidation of unsaturated hydrocarbons (C_2H_2 and C_3H_6). The introduction of a slight amount of manganese shifted the light-off curves toward lower temperatures. Based on the XPS results, the enhanced catalytic activity is thought to benefit from the abundant presence of oxygen vacancies in the doped oxide.

© 2012 Elsevier B.V. All rights reserved.

1. Introduction

Transition metal oxide systems with the general formula AB_2O_4 (both A and B are transition metal ions) are widely used as heterogeneous catalysts for several chemical reactions and have many important industrial applications [1,2]. Binary spinel-type oxides represent a key family of materials for such purposes and exhibit generally better performance relative to the simple mixture of the corresponding single oxides. In the past decades, the spinels of the $Co_{3-x}Mn_xO_4$ (CMO) series have attracted a great interest due to their attractive electronic, magnetic, optical, and catalytic properties [3–7]. More recently, mixed oxide of Co–Mn type was reported to present good catalytic performance for the oxidation of the volatile organic compounds (VOCs) [8]. VOCs are associated with various health-related problems, and catalytic oxidation is one of the most promising environmental technologies to reduce their emissions.

Manganese-rich phases ($Co_{3-x}Mn_xO_4$, $x \ge 1.4$) [9–11] and Co_2MnO_4 systems [5,6,12–16] were intensively investigated, while only few studies were devoted to the entire range [17,18] as well as to the cobalt-rich systems [7,19–22]. For example, Gautier et al. [20] reported that the Co^{2+}/Co^{3+} ratio increased with the manganese concentration increasing in the range of $0 \le x \le 1$. They found that manganese was mainly present as Mn^{3+} for samples prepared at 150 °C, while both Mn^{3+} and Mn^{4+} ions were detected for samples prepared at 400 and 1000 °C [20]. Moreover, Restovic et al. [21] reported the effect of manganese-doped cobalt oxide on the oxygen electro-reduction reactions. Later, the effect of manganese substitution, up to $x = 1.0$, on the crystal structures and dielectric properties of CMO spinels was investigated by Meena et al. [7]. They observed no significant change in the structural symmetry with increasing x up to 1.0, and attributed the linear increase in the lattice parameter with x to the substitution of Co^{3+} by Mn^{3+} [7]. Recently, Bordeneuve et al. [22] characterized the CMO spinels over the whole solid solution range, and gave the ion distribution as $Co^{2+}[Co^{2+}{}_aCo^{3+}{}_bMn^{3+}{}_cMn^{4+}{}_d]O_4{}^{2-}$. Although the physical properties of the cobalt-rich manganese spinels were understood to some extent, the knowledge of their catalytic activity upon deep oxidation of VOCs is scarce. As the physicochemical properties are

* Corresponding author. Tel.: +49 521 106 2199; fax: +49 521 106 6027.
E-mail address: zhenyu.tian@uni-bielefeld.de (Z.-Y. Tian).
[1] Present address: Department of Applied Physics, Technische Universiteit Eindhoven, 5600 MB Eindhoven, The Netherlands.
[2] Present address: Nanomaterials Research Unit, SAM Department, Centre de Recherche Public - Gabriel Lippmann L-4422 Belvaux, Luxembourg.

0926-3373/$ – see front matter © 2012 Elsevier B.V. All rights reserved.
doi:10.1016/j.apcatb.2012.01.013

directly related to the nature and stoichiometry of the bound metal ions in the final mixture, a systematic investigation of the configuration and site occupation at different compositions and their catalytic activity is desired.

Several methods have been used for the preparation of CMO films, such as thermal decomposition [14], reactive ion plasma sputtering [13], spray pyrolysis [20,21,23], the Pechini method [6], anodic electro-deposition [17], sol–gel [16,24], co-precipitation [11,22,25,26], the conventional solid-state reaction [7] and the ceramic method [9,19,27,28]. Compared to these methods, chemical vapor deposition (CVD) is particularly well adapted for the systematic preparation of pure and doped spinels [29–33] and perovskite oxides [34–36] on various kinds of substrates.

The current work is oriented toward investigation of the structure, electrical properties and catalytic activity of a series of cobalt-rich CMO films prepared by PSE–CVD. The deposited films are characterized by XRD, FTIR, Raman spectroscopy and XPS. The effect of manganese addition on the thermal stability and redox performance is studied. An attempt to correlate the electrical and catalytic behavior of CMO films with the nature and extent of ionic substitutions will be discussed.

2. Experimental

2.1. Preparation

The deposition of metal oxides was performed in a cold-wall stagnation point flow CVD reactor employing a pulsed-spray evaporation (PSE) unit for the delivery of the precursor liquid feedstock [35,37–39]. The detailed description of the deposition setup can be found in our previous work [30]. To obtain stoichiometric single-phase films and keep the precursors soluble in ethanol as the solvent, cobalt acetylacetonate ($Co(acac)_2$) and tris(2,2,6,6-tetramethyl-3,5-heptanedionato) manganese ($Mn(thd)_3$) were kept at respective concentrations of 10 and 5 mM. By adjusting the molar ratio of the two metallic elements, the two solutions were mixed to provide different blended feedstocks, which were kept at room temperature under atmospheric pressure during the deposition process. The PSE delivery was achieved with a valve opening time of 2.5 ms and a frequency of 4 Hz. The blended feedstock was injected as a fine spray into a 30 cm-long evaporation chamber kept at 210 °C. The resulting vapor was transported to the deposition chamber kept at 230 °C, with N_2/O_2 flow rates of 0.5/2 slm. Planar glass, silicon, stainless steel and mesh of stainless steel substrates were heated using a flat resistive heater to 400 °C during deposition and the total pressure in the reactor was kept at 32 mbar. The thickness of the deposited films was determined gravimetrically by measuring the weight change of the substrates with a microbalance (Mettler ME30, digital resolution of 1 μg). To differentiate the blended feedstock and the actual composition of the films, the compositions of $Co_{3-y}Mn_yO_4$ and $Co_{3-x}Mn_xO_4$ were used here (see Table 1), respectively.

2.2. Characterization

Several techniques were used to characterize the deposited films, including X-ray diffraction (XRD), Fourier transform infrared (FTIR) and Raman scattering spectroscopy. A Phillips X'Pert Pro MDR diffractometer with PW3830 X-ray generator (Cu Kα radiation, λ = 0.154056 nm) was employed, operating at 40 kV and 30 mA. Data were recorded in a 2θ range from 20° to 80°, with a scanning step of 0.05°. By referring to the powder XRD database (JCPDS-ICDD), the crystalline phases were identified. A FTIR spectrometer (Nicolet FTIR 5700) and a home-built Raman spectrometer with respective spectral resolutions of 2 and 4 cm^{-1} were used to confirm the spinel structure of the oxides. Related details to the Raman measurements have been reported elsewhere [40].

X-ray photoelectron spectroscopy (XPS) was used to monitor the chemical states of the constituent elements, using a Thermo Fisher Scientific apparatus with a Al Kα line radiation source at a base pressure of 3×10^{-8} mbar. The charge-shifted spectra were calibrated using the C1s photoelectron signal at 284.7 eV. Elemental quantification was achieved by using the atomic sensitivity factors provided by the manufacturer, and the peak deconvolution was estimated by curve fitting using Gaussian–Lorentzian line shapes after a nonlinear background subtraction.

To illustrate the redox properties of the $Co_{3-x}Mn_xO_4$ films grown on stainless steel substrates, a temperature-programmed reduction (TPR) followed by re-oxidation (TPO) were carried out from 100 to 600 °C with a temperature ramp of 3 °C/min, under an argon flow of 0.05 L/min containing respective 5 vol.% of H_2 (TPR) or O_2 (TPO). Since the spinel crystalline phase is active for the deep oxidation of hydrocarbons and not the monoxide phase, it does make sense to tract the integrity of the spinel in reducible conditions and its regeneration in oxidizing conditions. During the TPR/TPO analyses, the IR emission spectra were recorded continuously and characteristic bands were integrated versus temperature to discuss the redox properties. With this technique, the sensitivity limited by detecting tiny changes in the dynamically renewed gas in conventional method is substantially improved. PC-controlled four-probe DC equipment was used to measure the electrical resistivity in the temperature range of 27–450 °C, in open air under ambient conditions.

2.3. Surface reactivity

Small unsaturated molecules, such as acetylene (C_2H_2) and propene (C_3H_6), are often encountered emissions from hydrocarbon flames and quite difficult to oxidize. In this work, the catalytic behavior of Co_3O_4 and of a sample with $y = 0.5$ was investigated toward the oxidation of the two hydrocarbons at atmospheric pressure in a fixed bed quartz reactor with 12 mg catalyst grown as thin film on meshes of stainless steel. The experimental setup has been described in detail elsewhere [32]. A feed of 2 vol.%

Table 1
Characteristics of $Co_{3-x}Mn_xO_4$ (CMO, $0 \le x \le 0.34$) spinel structures.

Feedstock ($y/Co_{3-y}Mn_yO_4$)	C_{Mn}[a] ($x/Co_{3-x}Mn_xO_4$)	Growth rate (Å/min)	a[b] (Å)	Volume (Å^3)
0.0	0.00	4.17	8.07008	525.57
0.05	0.035[c]	4.12	8.07415	526.37
0.1	0.08[c]	4.09	8.07736	526.99
0.2	0.12[c]	4.07	8.08176	527.86
0.3	0.183	4.08	8.08728	528.94
0.4	0.293	3.90	8.09290	530.04
0.5	0.34	3.73	8.09860	528.64

[a] C_{Mn} is the manganese content (x) in $Co_{3-x}Mn_xO_4$ films obtained by XPS.
[b] a represents the lattice parameter.
[c] These values are obtained from extrapolation.

C_2H_2/C_3H_6, 20 vol.% O_2 and the balance of argon were introduced into a tubular glass reactor (9.0 mm inner diameter) at a total flow rate of 0.015 L/min. Flow rates of gases were controlled by MKS mass-flow controllers, whereas the temperature of the reactor was raised with a ramp of 3 °C/min using a HT60 controller (Horst). The temperature of the mesh inside of the reactor was recorded using K-thermocouples and a digital thermometer (Greisinger GMH3250). The exhaust gases were analyzed using a homemade KBr-transmission cell and an FTIR spectrometer in the wavelength range of 400–4000 cm^{-1}.

2.4. Data treatment

The fuel conversion was calculated as follows:

$$\text{Fuel conversion\%} = \frac{X_{\text{fuel}}(\text{inlet}) - X_{\text{fuel}}(\text{outlet})}{X_{\text{fuel}}(\text{inlet})}, \quad (1)$$

where X_{fuel} (inlet) and X_{fuel} (outlet) are the fuel mole fractions in the inlet and exhaust streams, respectively.

According to the Bouguer–Beer–Lambert's law, the intensity of the characteristic peak (I) in the FTIR spectra is proportional to the absorption coefficient (A_c), light path length (L) and partial pressure of the specific species (P), as shown in Eq. (2).

$$I = A_c \times L \times P \quad (2)$$

For a specific species A, the absorption coefficient and light path length are fixed, thus its intensity ratio at temperature i ($I_{A,i}$) and j ($I_{A,j}$) should be equal to its mole ratio at position i ($M_{A,i}$) and j ($M_{A,j}$):

$$\frac{I_{A,i}}{I_{A,j}} = \frac{M_{A,i}}{M_{A,j}} \quad (3)$$

For the current system, the mole number of propene can be calculated:

$$M_{\text{fuel},i} = \frac{M_{\text{fuel},0} \times I_{\text{fuel},i}}{I_{\text{fuel},0}} \quad (4)$$

where $M_{\text{fuel},0}$ and $I_{\text{fuel},0}$ stand for the mole number and integrated intensity of fuel (C_2H_2 or C_3H_6) at inlet condition. According to the carbon balance, the quantity of CO_2 when the fuel is completely converted ($M_{CO_2,f}$) can be calculated with $M_{\text{fuel},0}$ and the chemical equation:

$$C_xH_y + \left[x + \left(\frac{y}{4}\right)\right] O_2 = xCO_2 + \frac{y}{2}H_2O \quad (5)$$

The number of moles of CO_2 at temperature i ($M_{CO_2,i}$) can be obtained as:

$$M_{CO_2,i} = \frac{M_{CO_2,f} \times I_{CO_2,i}}{I_{CO_2,f}} \quad (6)$$

By applying (2), the intensity ratio of CO and CO_2 can be written as:

$$\frac{I_{CO,i}}{I_{CO_2,i}} = \left[\frac{A_c(CO)}{A_c(CO_2)}\right] \times \left[\frac{M_{CO,i}}{M_{CO_2,i}}\right] \quad (7)$$

With the calibration of known ratios CO/CO_2 and CH_4/CO_2, the ratio of $A_c(CO)/A_c(CO_2)$ and $A_c(CH_4)/A_c(CO_2)$ were calculated and accordingly, CO and CH_4 could be quantified at each temperature position.

3. Results and discussion

3.1. Growth and structure

By varying the temperature in the range of 250–450 °C, the effect of the substrate temperature on the growth rate of Co_3O_4 was investigated, and the best performance was noticed at 400 °C. To compare the characteristics, including the growth rate, refined lattice parameter, the calculated cell volume, density and film composition summarized in Table 1, all films were deposited to have an approximate thickness of 320 nm at the fixed substrate temperature of 400 °C. The film composition was controlled by adjusting the liquid feedstock composition. As seen from Table 1, the growth rate displays a global decrease with manganese insertion, which could result from the relatively low growth rate of Mn_3O_4 under our experimental conditions.

With XRD, FTIR and Raman spectra, all deposited films were revealed to present a single-phase cubic spinel structure, and the manganese incorporation was indicated by observing the typical peaks shift upon the increase of the manganese concentration in the blended feedstock up to $y = 0.5$, as displayed in Fig. 1. The XRD patterns of the oxides grown on silicon substrate are shown in Fig. 1(a). The diffraction peaks of non-doped Co_3O_4 film were detected at $2\theta = 31.40°$, 36.93°, 38.63°, 44.85°, 59.40° and 65.39°, corresponding to respective crystallographic planes (2 2 0), (3 1 1), (2 2 2), (4 0 0), (5 1 1) and (4 4 0) of Co_3O_4 spinel (JCPDS No. 74-1656) with the symmetry group $Fd3m$. No peaks corresponding to impurity phases such as CoO and Co_2O_3 were detected. With manganese incorporation in the feedstock up to $y = 0.5$, no obvious

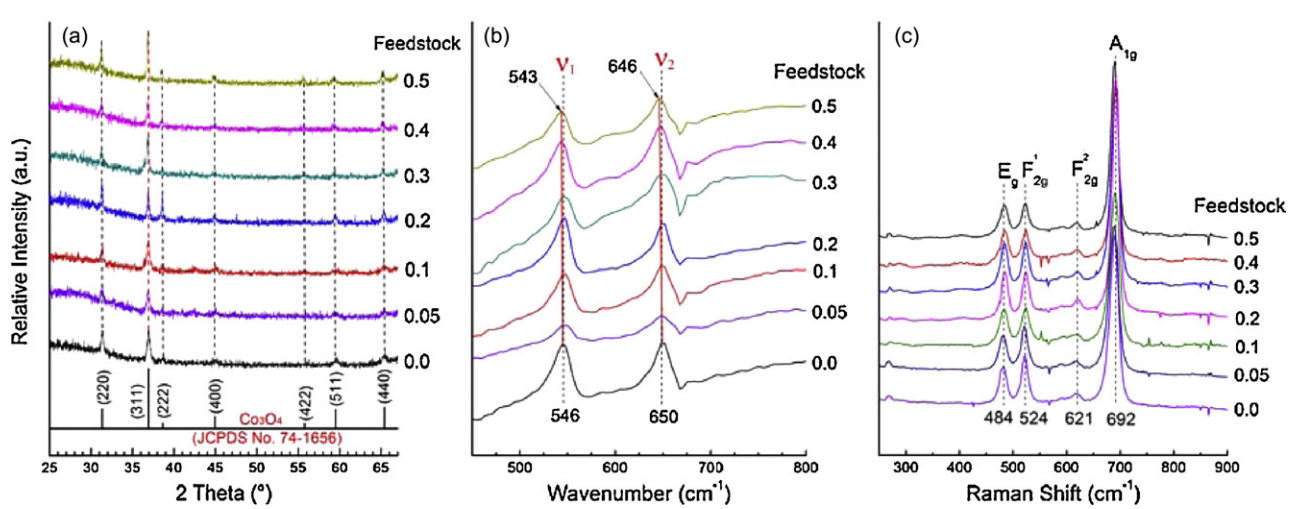

Fig. 1. XRD patterns of the structured CMO mixed oxides deposited on silicon substrate (a); FTIR specular reflectance spectrum (b); and Raman spectra at 27 °C (c) of the spinel structure as a function of manganese incorporation.

change was observed except a small shift in peaks positions toward lower diffraction angles, confirming that the prepared oxides crystallize in the face-centered cubic system of spinel type, which is in accordance with previous conclusions given by both Meena et al. [7] and Liang et al. [16].

The structure of the CMO samples was studied by FTIR emission spectroscopy at 140 °C, as depicted in Fig. 1(b). For Co_3O_4, two strong and sharp bands located at around 650 cm^{-1} and 546 cm^{-1} corresponding to the ν (Co–O) modes were observed, in good agreement with our previous work [30]. The two bands tend to show a small shift toward lower wavenumbers with the increase of the manganese concentration in the feedstock. According to Askarinejad and Morsali [41], the two bands at around 600 cm^{-1} and 500 cm^{-1} are characteristic of ν (Mn–O) modes of Mn_3O_4. Thus the shift comes from the progressive incorporation of manganese into the cubic structure, which supports the XRD results.

Fig. 1(c) displays the Raman spectra of the CMO films as a function of manganese incorporation. Starting with the pure cobalt oxide, four well-defined peaks are located at 484, 524, 621 and 692 cm^{-1}, whose positions and widths are consistent with previous reports for the spinel of Co_3O_4 [37,42,43]. In the frequency range of 200–700 cm^{-1}, the normal spinel structure of Co_3O_4 possesses four Raman-active modes depicted as $A_{1g} + E_g + 2F_{2g}$. The high-frequency band at 692 cm^{-1}, corresponding to the A_{1g} mode, is attributed to the octahedral sites [CoO_6] in the O_h^7 symmetry. The weak band at 621 cm^{-1} can be assigned to the F_{2g} mode, whereas the Raman modes at 524 cm^{-1} and 484 cm^{-1} have respective symmetries of F_{2g} and E_g, and result from the vibration of tetrahedral and octahedral sites [44]. As reported in previous work, the room-temperature Raman spectrum of Mn_3O_4 sample exhibits five peaks, an A_{1g} symmetry mode at 660 cm^{-1}, T_{2g} symmetry modes at 479 cm^{-1} and 375 cm^{-1}, an E_g symmetry mode at 320 cm^{-1}, and a T_{2g} symmetry mode at 290 cm^{-1} [45–48]. Upon increase of y from 0 to 0.5, the strongest band, A_{1g}, slightly shifts to lower wavenumbers, indicating the incorporation of manganese into the lattice.

The actual manganese concentration in the mixed oxides was revealed by the XPS analysis after surface cleaning using an Ar ion beam. Fig. 2(a) depicts the composition results obtained for pure and doped films (y = 0.3–0.5) as a function of manganese concentration in the feedstock. The observed trend exhibits a linear relation with the feedstock. It should be noted that the doped samples tend to have a lower manganese concentration than the liquid feedstock. For y = 0.5, the film composition is measured to be 0.34 in the deposited sample. Such phenomenon results from different sticking coefficients between cobalt and manganese precursors.

The variation of the lattice parameter confirms the manganese insertion into the films. As displayed in Fig. 2(b), a linear increase from 8.070 to 8.099 Å is noted with manganese doping, which agrees with Vegard's law. Two substitution mechanisms could account for the expansion of the unit cell. The first one is the progressive substitution of Co^{3+} ions ($r_{CO}^{3+} = 0.545\,Å$, trivalent with low spin [49]) at the octahedral (B) site by Co^{2+} ($r_{CO}^{2+} = 0.745\,Å$, octahedral coordination, divalent with high spin) and Mn^{4+} ($r_{Mn}^{4+} = 0.53\,Å$, octahedral coordination). The other possibility would be the replacement of Co^{3+} by Mn^{3+} ions ($r_{Mn}^{3+} = 0.645\,Å$, octahedral coordination, trivalent with high spin). The two pathways will be further discussed based on the results of the XPS analysis. By applying the Debye–Scherrer formula to the two most intense diffraction peaks, the average crystallite size was determined to be about 22 nm, and the manganese incorporation has no significant influence. Further evidence about the progressive incorporation of manganese into the mixed oxides can be provided by the linear shift of the two characteristic bands in the emission FTIR spectra, as presented in Fig. 2(c).

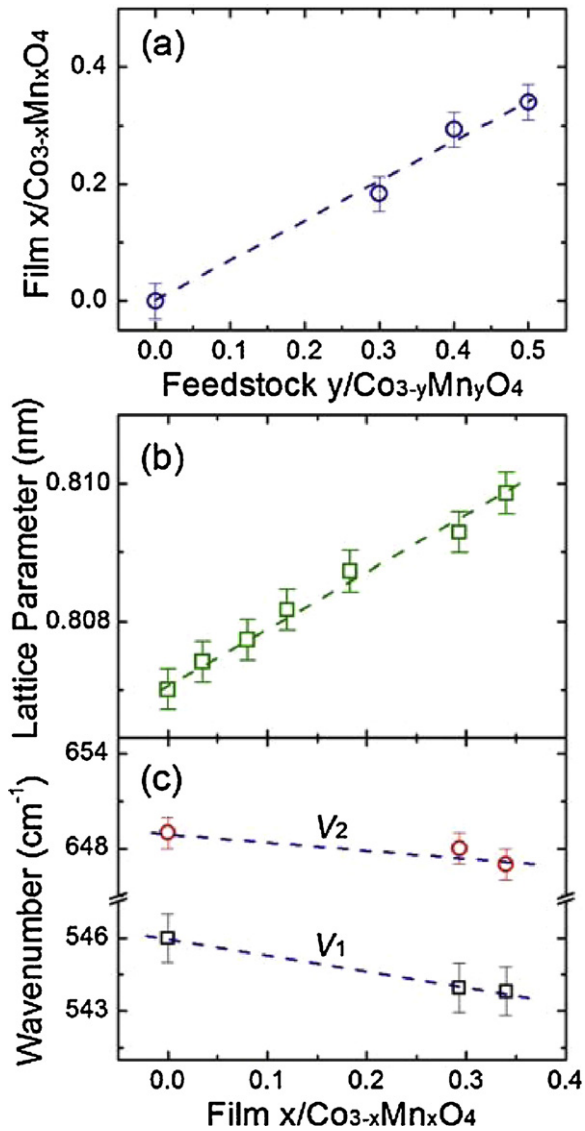

Fig. 2. Control of the film composition by varying the feedstock (a); variation of the lattice parameter of the spinel structure as a function of manganese incorporation (b); the effect of manganese insertion on the vibration frequency of the characteristic bands in FTIR emission spectrum (c).

3.2. Cationic distribution

The oxidation states of the constituent elements Co, Mn and O ions in the deposited CMO spinels were assessed by ex situ XPS with an emphasis on the peaks associated with Co 2p and Mn 2p. Surface contaminations were inherent to ex situ analysis. These contaminations were etched to a large extent using 20 s of argon ion beam. The relative intensities of the photoelectron peaks of Co 2p and Mn 2p, collected in Fig. 3, are obtained after Ar etching. Details regarding the data fit and the bulk cationic distributions are summarized in Table 2.

For manganese-free oxide, the binding energy of Co $2p_{3/2}$ is 779.53 eV and the spin-orbital splitting is ΔE = 15.11 eV. These values are in the range of those reported for pure cobalt oxide [3,48,50]. With the procedure similar to that of Restovic et al. [21], the Co 2p spectra were deconvoluted into two spin-orbit doublets D_1 and D_2 and three satellite peaks (S_1 to S_3). D_1 and D_2 were constrained to the full width at half maximum (FWHM) at 1.32 and 2.57 eV, respectively. The satellite peaks S_1 and S_2, corresponding to octahedral sites, were constrained to a FWHM of 4.43 and 7.47 eV, respectively.

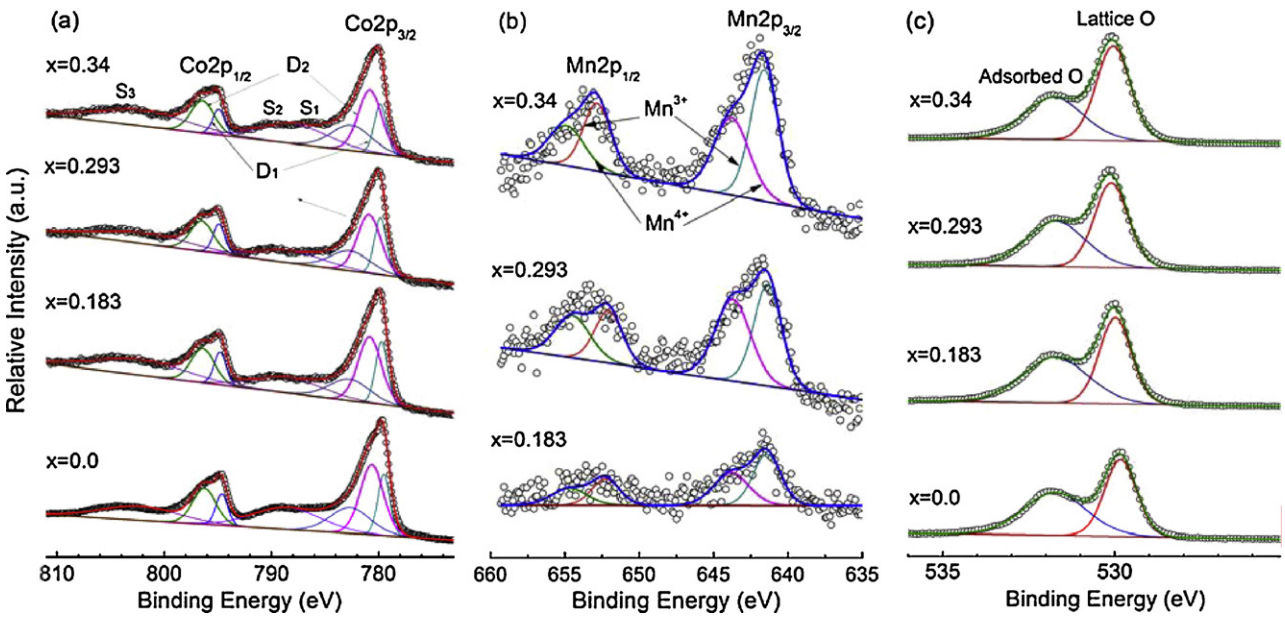

Fig. 3. XPS analysis of the Co and Co–Mn samples: fitted Co $2p_{1/2}$ and Co $2p_{3/2}$ photoelectron peaks (a); fitted Mn $2p_{1/2}$ and Mn $2p_{3/2}$ photoelectron peaks (b); fitted O1s photoelectron peaks (c).

The S_3 peak corresponds to tetrahedral sites and was restricted to a FWHM of 10.12 eV. The fitted ratio of Co^{3+}/Co^{2+} in cobalt oxide is 1.996, which is very close to the expected value. With manganese doping, all films exhibit Co $2p_{3/2}$ and Co $2p_{1/2}$ peaks at 779.9–779.4 and 795.5–794.6 eV, respectively, which is consistent with a previous study [21]. The Co^{3+}/Co^{2+} ratio in the films was noted to decrease with manganese doping concentration. The concentration increase of Co^{2+} suggests that the first postulated substitution mechanism where Co^{3+} is replaced by Co^{2+} and Mn^{4+} is likely. We would like to mention that a similar decreasing trend was detected for CMO samples prepared by spray pyrolysis [23], which confirms the intrinsic nature of this substitution mechanism.

Table 2
XPS relative intensity and bulk cationic distributions of the CMO oxides ($0 \le x \le 0.34$).

Relative intensity		x			
		0.00	0.183	0.293	0.34
Co^{3+} (%)	D_1(Co $2p_{3/2}$)	9.82	8.96	11.64	11.04
	D_1(Co $2p_{1/2}$)	9.95	9.08	11.79	11.2
	S_1	10.05	10.05	8.98	8.35
	S_2	13.75	13.29	9.04	10.22
Co^{2+} (%)	D_2(Co $2p_{3/2}$)	21.76	21.92	23.34	22.53
	D_2(Co $2p_{1/2}$)	22.06	22.21	23.65	22.85
	S_3	12.16	14.49	11.55	13.82
Co^{3+}/Co^{2+} [a]		1.996	1.635	1.590	1.364
Mn^{3+} (%)	Mn $2p_{3/2}$	–	27.42	24.47	28.33
	Mn $2p_{1/2}$	–	22.39	25.33	21.51
Mn^{4+} (%)	Mn $2p_{3/2}$	–	27.63	24.66	28.56
	Mn $2p_{1/2}$	–	22.56	25.53	21.60
Mn^{3+}/Mn^{4+}		–	1.24	0.95	2.56
Cationic distributions	Co^{2+}	1.0	1.07	1.05	1.13
	Co^{3+}	1.996	1.75	1.66	1.53
	Mn^{3+}	–	0.10	0.14	0.24
	Mn^{4+}	–	0.08	0.15	0.10
Composition	C1s	43.94	34.87	34.57	31.17
	O1s	40.32	48.15	49.32	53.38
	Co 2p	15.74	16.19	14.54	13.7
	Mn 2p	0.0	0.79	1.57	1.75
O/(Co + Mn)		2.56	2.84	3.06	3.46

[a] The ratio of Co^{3+}/Co^{2+} is calculated based on the formula $[D_1(\text{Co } 2p_{3/2}) - D_1(\text{Co } 2p_{1/2}) + S_1 + S_2)]/[D_2(\text{Co } 2p_{3/2}) - D_2(\text{Co } 2p_{1/2}) + S_3]$.

Fig. 3(b) displays the XPS spectra in the Mn 2p region for the Mn-doped films. In general, the Mn 2p peaks are composed of two main spin-orbital lines, Mn $2p_{3/2}$ and Mn $2p_{1/2}$ peaking at 641.1 and 652.4 eV, separated by about 11.3 eV, in agreement with previous XPS spectra of Mn 2p reported by Todorova et al. [51]. The deconvolution of the Mn 2p was performed by constraining the FWHM of Mn^{4+} and Mn^{3+} to 2.81 and 2.19 V, respectively. The observation of these two cations also evidences the mechanism that cobalt cations are substituted by Mn^{3+} and Mn^{4+}. It was postulated that Mn^{4+} could be formed in the Co–Mn oxide prepared at higher temperature [52]. The use of 400 °C for deposition in this work could contribute to the formation of Mn^{4+} in the octahedral sites, in accordance with the proposition of Rios et al. [23]. For $Co_{2.817}Mn_{0.183}O_4$ and $Co_{2.707}Mn_{0.293}O_4$, the ratios of Mn^{3+}/Mn^{4+} are quite close. However, this ratio increases about twice for $Co_{2.66}Mn_{0.34}O_4$. Bordeneuve et al. [22] obtained similar results for CMO spinels of $x = 0.28$ and 0.34.

In the XPS spectra of O1s shown in Fig. 3(c), asymmetric two-band structures were observed for all the samples. Based on previous reports concerning cobalt oxides [53,54], the dominant peak at lower binding energy of about 529.8 eV is characteristic of lattice oxygen and the minor peak at higher binding energy of 531.8 eV is assigned to the chemisorbed or dissociated oxygen or hydroxyl species. With manganese doping, the ratio of O/(Mn + Co) increases. Based on the components given in Table 2 and to satisfy the electroneutral criterion, the oxygen vacancies were calculated to show an increase from 1.12 for the non-doped sample to 2.92 in the sample with $x = 0.34$. It has been established that the presence of oxygen vacancies is of importance for physical property changes of the materials as well as for their catalytic applications.

3.3. Thermal properties

Thermal stability is a very desirable property of catalysts in most of their applications. Manganese plays a significant role for the thermal stability of oxide catalysts and it was proved to act as a stabilizer for the spinel of cobalt oxide [26,55]. The thermal properties of the CMO films were studied with FTIR emission spectroscopy under

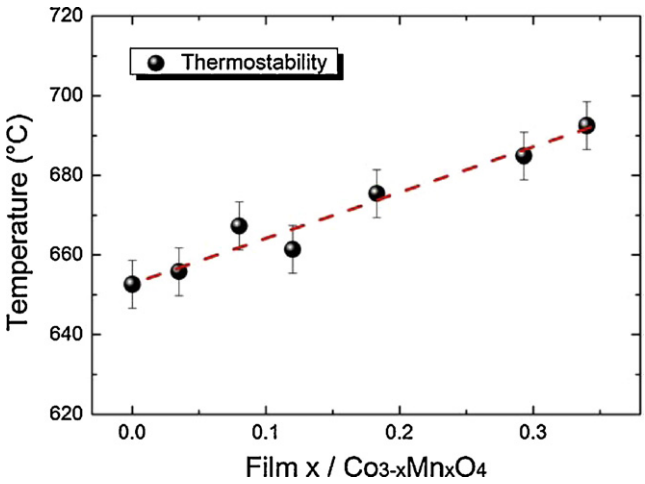

Fig. 4. The effect of Mn-doping on the thermal stability on the CMO spinel structures.

ambient atmosphere and using a temperature-programmed mode [30,37]. As shown in [30], the lattice stability can be determined by integrated intensity of the feature peaks of the spinel as a function of the temperature which reflects the phase transformation. Fig. 4 presents the upper stability limit of the spinel as a function of the amount of incorporated manganese. As shown in this plot, manganese insertion improves the thermal stability of the spinel. Cobalt oxide decomposes to give rise to cobalt monoxide at about 650 °C, supporting previously reported results [30]. From cobalt oxide to the Mn-doped spinel with $x = 0.34$, the upper stability limit was shifted by about 40 °C in a linear way, indicating that the use of low manganese concentration favors the formation of spinel-type phases with high thermal stability by the substitution of Co with Mn. As indicated in the catalytic oxidation process of methane [29], the specific reaction rate increased exponentially as a function of temperature. The improvement of 40 °C in the upper stability limit is particularly interesting for catalytic oxidation since a small increase of the temperature would lead to a substantial increase of the reaction rate. Zhang et al. [55] suggested that the presence of Mn caused the formation of smaller CMO solid solution particles and increased the amount of active oxygen, both contributing to promote the stability of CMO. In this work, the increase of oxygen content is confirmed by the XPS analysis (see Table 2). Moreover, the increase of the thermal stability limit could come from the introduction of ion groups such as OH^- in the current case, the presence of which can be a factor that enhances the stability of the unusual cation distribution.

Compared to other doped cobalt-rich binary spinels, CMO presents a good performance in terms of stability at high temperatures. The thermal stability of CMO in the present work are generally higher than those of Ni-doped Co_3O_4 reported in our previous studies [30], which agrees with the statement that the cobalt manganites have a higher thermal stability than the cobaltites of Ni, Cu and Zn given by Klissurski and Uzunova [56]. Bahlawane et al. [37] have studied the thermal stability of iron-doped cobalt oxide and a much higher iron composition (0.65) was needed to achieve a similar increase of thermal stability. They also compared the thermal stability of doped Co_3O_4 with various transition metals including Fe, Ni, Zn and Cr and concluded about the superiority of $Co_{3-x}Zn_xO_4$ and $Co_{3-x}Cr_xO_4$ [37]. This pool can be enriched by the addition of manganese. Thus, from the thermal stability point of view, CMO shows a competitive potential in high-temperature applications such as catalytic oxidation of hydrocarbons.

3.4. Redox behavior

To evaluate the reducibility and re-oxidibility as a function of the composition, both TPR and TPO were carried out with 320 nm-thick CMO films. Fig. 5 summarizes the influence of manganese content on the TPR and TPO profiles of various samples by integrating the two specific emission bands of the spinel structures obtained with FTIR spectroscopy. The temperature T_{50}, at which

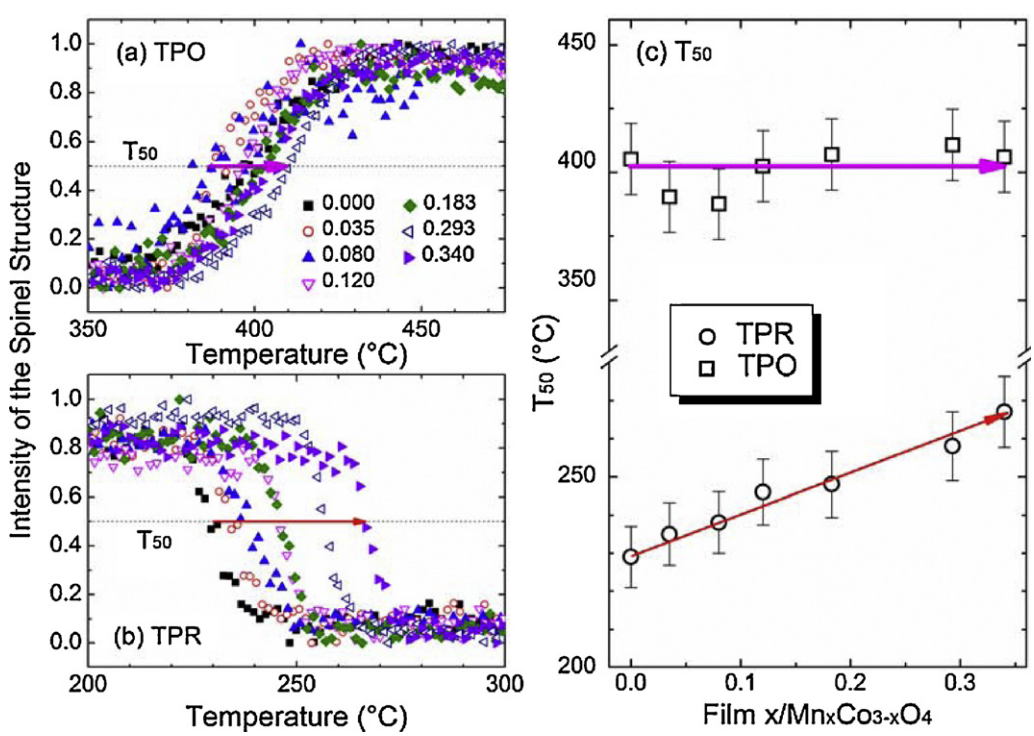

Fig. 5. TPR and TPO patterns at Ramp of 3 °C/min of CMO spinel structures. The intensity of the spinel structure was estimated by integrating the area under the emission bands ν_1 and ν_2 as a function of the temperature.

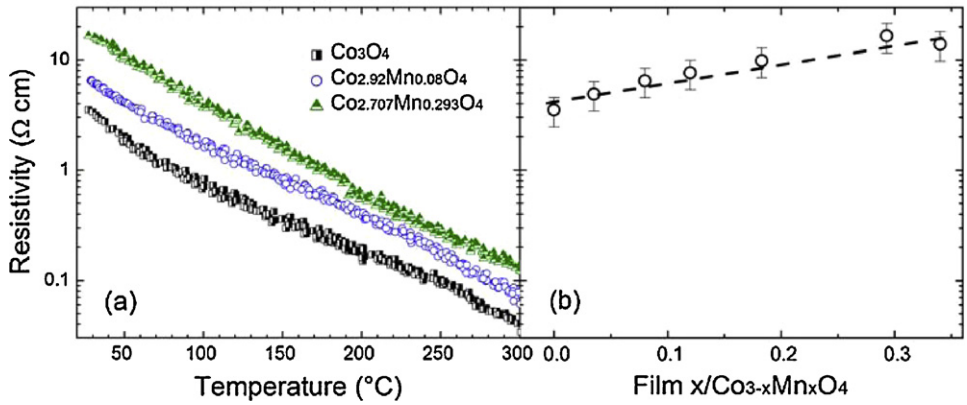

Fig. 6. Temperature dependence of resistivity for CMO spinels (a) and comparison of their values at 27 °C (b).

50% of the emission bands were formed (TPO) or depleted (TPR), was used to analyze the effect of Mn doping.

Manganese insertion into the spinel structure of cobalt oxide tends to induce a systematic shift of the reduction toward higher temperatures. As shown in Fig. 5(b), the integrity of the spinel Co_3O_4 is affected starting at 223 °C and the spinel is completely reduced at 242 °C, corresponding to the reduction steps of Co_3O_4 to CoO. The manganese-doped sample $x = 0.12$ displays lower reducibility with the two temperatures shifting to 239 and 255 °C, respectively. The shift of these temperatures is more pronounced, 262 and 277 °C, for highly doped spinel $x = 0.34$, indicating a much lower reducibility. Our previous work related to iron [33,37] and zinc [57] insertion to the cobalt oxide spinels shows a similar behavior. Feldmann et al. [57] suggested that Zn doping may cause an insertion of hydrogen atoms into the lattice during deposition and then limit the mobility of the oxygen atoms. This could also occur in the current case. As proposed by Wyrwalski et al. [58], anionic vacancies that can separate two Co_3O_4 species were formed upon dispersion of Co_3O_4 on ceria. In this work, this kind of vacancies can also be generated upon manganese incorporation and make the corresponding samples less reducible. Compared to the reduction process, only a minor shift is observed in the case of re-oxidation. The determining step of the re-oxidation is the reaction of oxygen with metal monoxide giving birth to spinel, while vacancies play key roles in the TPR process. The effect of manganese insertion on the reducibility and re-oxidibility can be easily seen from T_{50}, as shown in Fig. 5(c). An increase of 40 °C is obtained for TPR_{50} from $x = 0$ to $x = 0.34$, whereas a 10 °C data scattering was observed for TPO_{50}.

3.5. Electrical resistivity

Fig. 6 displays the electrical resistivity (ρ) of the CMO films deposited on glass substrates as a function of manganese insertion in the temperature range of 27–300 °C. For the sake of clarity, only profiles of samples with $x = 0$, 0.08 and 0.293 are shown. The electrical resistivity was generally found to decrease exponentially with increasing temperature over the entire temperature range, exhibiting semiconductor-like behavior. The manganese introduction leads to the increase of electrical resistivity. The electrical resistivity of the Mn-free sample at room temperature is 3.51 Ω cm, as seen in Fig. 6(b), which compares well with that of films prepared by sol–gel [24]. By incorporating manganese up to $x = 0.34$, the room-temperature electrical resistivity of the films shows generally an increase up to a value of 16.50 Ω cm, which is about five times that of the pure cobalt oxide. In general, the magnitude of the increase in the electrical resistivity is more pronounced at low temperature. Scattering of the charge carrier by manganese doping is presumably the effect leading to the increase of the electrical resistivity. In previous work, Verwey [59] proposed the electrical conduction mechanism of spinel oxides by polaron jumps between neighboring octahedrally coordinated cations. Similarly to the Co–Ce–O system [58], the anionic vacancies close to the Mn cations can be suitable sites to trap oxygen species, which can then stretch the distance between the two Co^{3+} ions located at the octahedral sites and lead to the increase of the electrical resistivity.

3.6. Catalytic activity

The grown CMO were tested toward the total oxidation of unsaturated hydrocarbons by selecting C_2H_2 and C_3H_6 as illustrative examples. To exclude the background effect of the mesh structures on the oxidation process, oxidation was also performed on non-coated mesh. The light-off curves of the samples are presented in Figs. 7 and 8 and summarized in Table 3. Fig. 7 compares the temperature-dependent conversion of C_2H_2 and C_3H_6 over $Co_{3-x}Mn_xO_4$ films and non-coated mesh. The detailed outlet

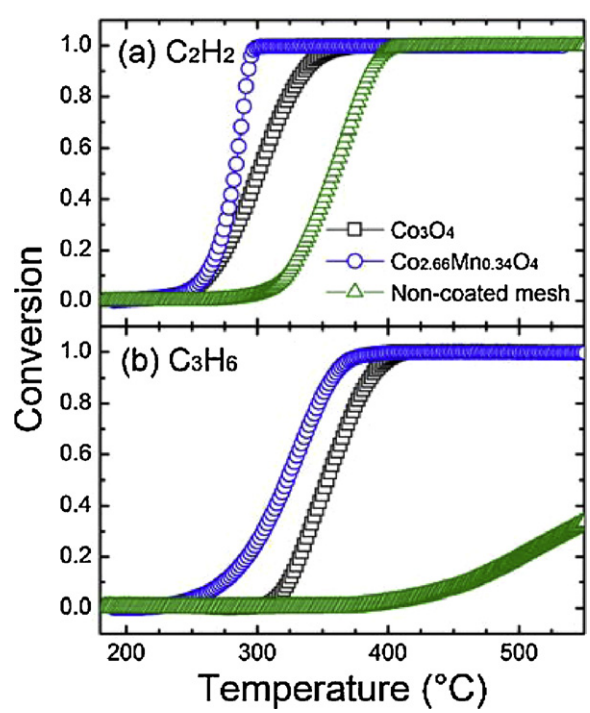

Fig. 7. Light-off curves of C_2H_2 and C_3H_6 over CMO ($x = 0$ and 0.34) spinel structures grown on mesh of stainless steel substrates and non-coated mesh.

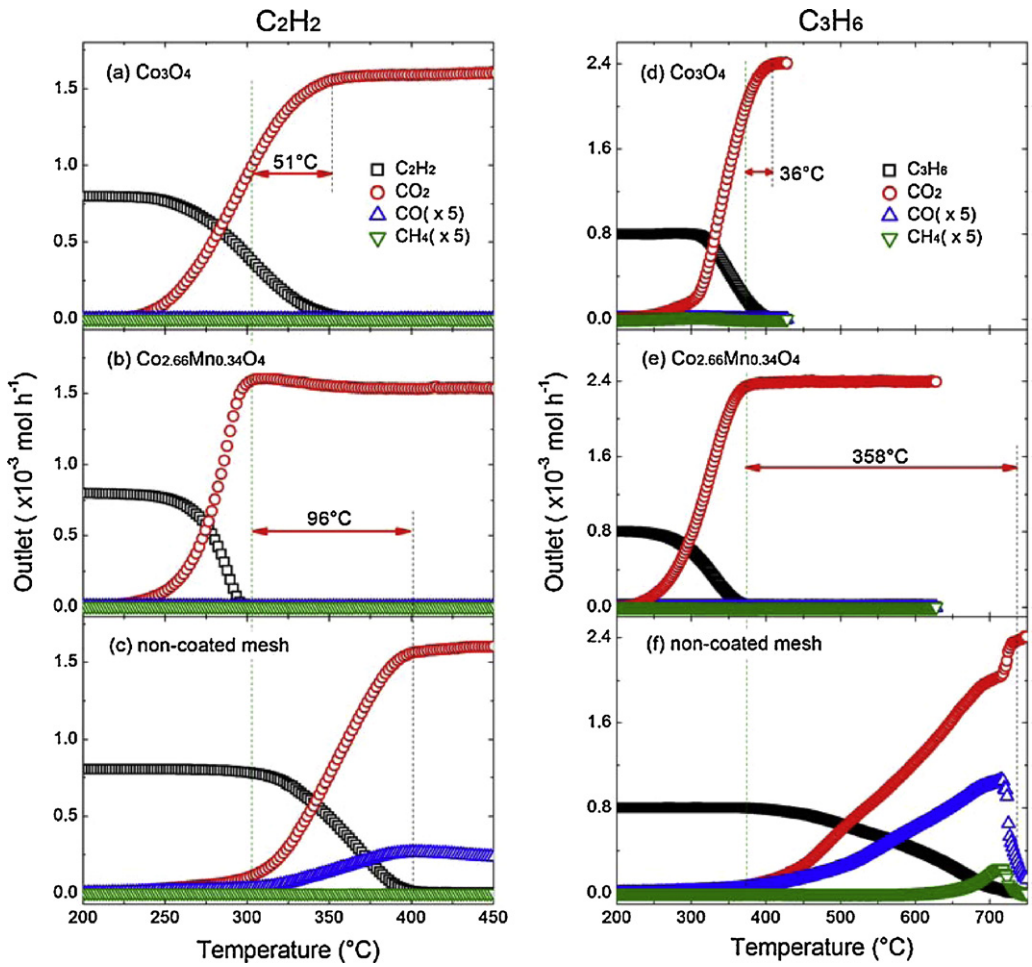

Fig. 8. Production profiles of C_2H_2/C_3H_6, CO, CO_2 and CH_4 in the oxidation of C_2H_2 and C_3H_6 over CMO (x = 0 and 0.34) spinel structures grown on mesh of stainless steel substrates and non-coated mesh.

profiles of the fuels and products are given in Fig. 8. The temperatures T_{50}, T_{90}, $T_{50}CO_2$ and $T_{90}CO_2$, corresponding to the fuel conversion and CO_2 selectivity, were selected as parameters to indicate the catalytic activity of the deposited samples toward hydrocarbons deep oxidation, as shown in Table 3. The catalytic performance improves from Co_3O_4 to $Co_{2.66}Mn_{0.34}O_4$, and both are superior to the non-coated mesh. It is worth noting that the catalytic oxidation of acetylene and propene under O_2-rich conditions is tested to have no obvious effect on the catalyst structure by comparing the obtained XRD spectra before and after the catalytic tests.

The selectivity-conversion plots show clearly that the investigated coatings favor the total oxidation of both unsaturated hydrocarbons at lower temperatures relative to the non-coated mesh. For C_2H_2, T_{50} and T_{90} were observed at 355 and 386 °C over non-coated mesh, whereas these values decreased by respective 56 and 51 °C over cobalt oxide and further decreased by 17 and 41 °C over $Co_{2.66}Mn_{0.34}O_4$, which reveals that the catalyst with small amount of manganese content shows the highest activity (see Fig. 7 and Table 3). Tian et al. [32] reported that T_{50} of C_2H_2 oxidation with Co_3O_4 deposited on monolithic cordierite support was 297 °C, which is in good agreement with the current Co_3O_4 sample prepared on mesh. Note that the T_{50} of C_2H_2 (282 °C, Table 3) with $Co_{2.66}Mn_{0.34}O_4$ in the current work is quite close to the value (280 °C) reported by Ivanova et al. [60] who used Au/Al_2O_3, revealing that $Co_{2.66}Mn_{0.34}O_4$ prepared by CVD features a competitive activity. The low-temperature shift of the light-off curve is more pronounced for C_3H_6 since the T_{90} difference between the non-coated mesh and $Co_{2.66}Mn_{0.34}O_4$ is 336 °C, demonstrating that $Co_{2.66}Mn_{0.34}O_4$ is very active for the total oxidation of propene and supporting the conclusion of Liang et al. [16] who reported that the

Table 3
Catalytic oxidations of C_2H_2/C_3H_6 over CMO catalysts grown on mesh of stainless steel substrates and non-coated mesh.

Fuel	Catalyst	T_{50} (°C)[a]	T_{90} (°C)[a]	$T_{50}CO_2$ (°C)[b]	$T_{90}CO_2$ (°C)[b]	E_a (kJ mol^{-1})[c]
C_2H_2	Non-coated mesh	355	386	356	387	168.97
	Co_3O_4	299	335	301	337	139.77
	$Co_{2.66}Mn_{0.34}O_4$	282	294	282	295	131.86
C_3H_6	Non-coated mesh	603	692	614	723	121.98
	Co_3O_4	354	385	356	387	158.32
	$Co_{2.66}Mn_{0.34}O_4$	321	356	323	357	114.59

[a] T_{50} and T_{90} represent the temperature at which the conversion of C_2H_2/C_3H_6 reaches 50% and 90%, respectively.
[b] $T_{50}CO_2$ and $T_{90}CO_2$ represent the temperature at which 50% and 90% conversion to CO_2 is reached.
[c] E_a is the apparent activation energy for the hydrocarbon oxidation at atmospheric pressure.

manganese insertion into the cobalt oxide spinel could enhance the catalytic activity of the oxidation of light olefins. Considering the higher activity, Mn-doped spinel of cobalt oxide could be a potential system for catalytic oxidation of hydrocarbons.

As presented in Table 3, the values of T_{50} and T_{90} of hydrocarbons conversion and those of CO_2 selectivity are almost identical for Co_3O_4. It is also the case for $Co_{2.66}Mn_{0.34}O_4$. However, differences are observed relative to non-coated mesh especially in the oxidation of C_3H_6, illustrating that a partial oxidation is occurred by generating products other than CO_2. This can be clearly seen in Fig. 8(f). With Co_3O_4 and $Co_{2.66}Mn_{0.34}O_4$, CO_2 is observed to be the only carbonaceous product and no secondary products are formed all over the entire oxidation process of C_3H_6, while CO and CH_4, coming from incomplete oxidation, were detected in addition to the production of CO_2 on non-coated mesh. Though some by-products are formed at certain temperatures for non-coated mesh, all indicate that CO_2 is the final product. Taking the temperature at which hydrocarbons are completely converted to CO_2 on $Co_{2.66}Mn_{0.34}O_4$ sample as a reference, Co_3O_4 and non-coated mesh show a respective increase of 51 and 96 °C for C_2H_2, and 36 and 358 °C for C_3H_6, which shows that the use of cobalt together with manganese can significantly affect the catalytic activity. By applying the Arrhenius equation in the conversion range within 15% [32], the apparent activation energies are calculated (see Table 3). In general, the manganese-doped cobalt oxide exhibits a lower activation energy. Compared to those activation energies obtained in the oxidation of C_2H_2 and C_3H_6 over Co_3O_4-coated monolith with a large flow rate (500 sccm) [32], the values obtained on Co_3O_4-coated mesh in this work are about 10 and 30 kJ mol^{-1} larger, the difference of which may come from the comprehensive effect of the support and inlet condition. Recently, Zhang et al. [55] and Aguilera et al. [8] also reported that the modification of Co_3O_4 by MnO_x could promote the preferential oxidation of CO, toluene and alcohols at lower temperatures.

The catalytic oxidation of the two hydrocarbons employing CMO systems consists of two irreversible steps, namely the reaction of the hydrocarbon with the lattice or trapped oxygen leading to its reduction and release of oxygen from the surface of the metal oxide, and the re-oxidation of the partly reduced metal oxide site by means of oxygen in a subsequent step. The TPO results (Fig. 5) indicate that the manganese introduction does not really influence the bulk re-oxidation behavior of CMO. Considering the TPR and catalytic results which reveal that Co_3O_4 has higher reducibility but lower activity than $Co_{2.66}Mn_{0.34}O_4$, the formation of oxygen vacant site plays a key role in the redox mechanism, the importance of which was pointed out previously by Noller and Vinek [61]. According to the XPS results and the enhancement of the thermal stability, the amount of oxygen vacancy is increased upon manganese incorporation, which can then accelerate the oxidation process. Furthermore, the catalytic activity could also benefit from the substitution of cobalt with manganese that is more active and from the cooperative effect among metallic species by increasing the oxide-reduction sites.

4. Conclusion

Thin $Co_{3-x}Mn_xO_4$ spinel films were grown from $Co(acac)_2$ and $Mn(thd)_3$ at 400 °C by PSE–CVD. The effect of manganese doping on the structure of the deposited films were evaluated using XRD, XPS, FTIR, and Raman analyses. Structural study reveals that the films retain the cubic spinel crystal structure up to manganese doping concentration of $x = 0.34$. The introduction of manganese leads to a decrease of electrical conductivity and reducibility but promotes the thermal stability. The catalytic performance of Co_3O_4 and $Co_{2.66}Mn_{0.34}O_4$ films toward acetylene and propene oxidation was investigated. Both coatings suppress the formation of by-products such as CO and CH_4, favoring the selectivity toward CO_2 at low temperatures. The mixed oxide catalyst with $x = 0.34$ displays a remarkable improvement in terms of the activity, selectivity and stability, which can possibly be a result of the increase of oxygen vacancies. A small amount of manganese insertion ($x = 0.34$) into cobalt oxide spinel displays better behavior in terms of high-temperature stability and low-temperature activity relative to pure Co_3O_4.

Acknowledgments

Dr. Tian thanks the Alexander von Humboldt foundation for his research fellowship. The authors thank Mr. Harald Waterbör for the technical assistance and Ms. Marina Schenk for the helpful discussions.

References

[1] F. Kovanda, T. Rojka, J. Dobešová, V. Machovič, P. Beydička, L. Obalová, K. Jirátová, T. Grygar, J. Solid State Chem. 179 (2006) 812–823.
[2] M. Hamdani, R.N. Singh, P. Chartier, Int. J. Electrochem. Sci. 5 (2010) 556–577.
[3] W.F. Wei, W.X. Chen, D.G. Ivey, Chem. Mater. 30 (2008) 1941–1947.
[4] J. Philip, T.R.N. Kutty, Mater. Lett. 39 (1999) 311–317.
[5] P.A. Joy, S.K. Date, J. Magn. Magn. Mater. 210 (2000) 31–34.
[6] F.M.M. Borges, D.M.A. Melo, M.S.A. Camara, A.E. Martinelli, V. Soares, J.H. Araújo, F.A.O. Cabral, J. Magn. Magn. Mater. 302 (2006) 273–277.
[7] P.L. Meena, R. Kumar, C.L. Prajapat, K. Sreenivas, V. Gupta, J. Appl. Phys. 106 (2009) 024105.
[8] D.A. Aguilera, A. Perez, R. Molina, S. Moreno, Appl. Catal. B: Environ. 104 (2011) 144–150.
[9] R. Buhl, J. Phys. Chem. Solids 30 (1969) 805–812.
[10] J.L. Martin de Vidales, E. Vila, R.M. Rojas, O. García-Martínez, Chem. Mater. 7 (1995) 1716–1721.
[11] E. Vila, R.M. Rojas, J.L. Martin de Vidales, O. García-Martínez, Chem. Mater. 8 (1996) 1078–1083.
[12] J.L. Gautier, C. Cabezas, S. Barbato, Electrochim. Acta 26 (1981) 1377–1382.
[13] G.P. Vasil'ev, L.A. Ryabova, Thin Solid Films 66 (1980) 119–124.
[14] E. Rios, P. Lara, D. Serafini, A. Restovic, J.L. Gautier, J. Chil. Chem. Soc. 55 (2010) 261–265.
[15] S. Tamura, J. Phys. Soc. Jpn. 61 (1992) 752–753.
[16] Q. Liang, K.D. Chen, W.H. Hou, Q.J. Yan, Appl. Catal. A: Gen. 166 (1998) 191–199.
[17] W.F. Wei, W.X. Chen, D.G. Ivey, J. Phys. Chem. C 111 (2007) 10398–10403.
[18] H. Bordeneuve, C. Tenailleau, S. Guillemet-Fritsch, R. Smith, E. Suard, A. Rousset, Solid State Sci. 12 (2010) 379–386.
[19] B. Boucher, R. Buhl, R. Di Bella, M. Perrin, J. Phys. 31 (1970) 113–119.
[20] J.L. Gautier, E. Rios, M. Gracia, J.F. Marco, J.R. Gancedo, Thin Solid Films 311 (1997) 51–57.
[21] A. Restovic, E. Ríos, S. Barbato, J. Ortiz, J.L. Gautier, J. Electroanal. Chem. 522 (2002) 141–151.
[22] H. Bordeneuve, A. Rousset, C. Tenailleau, S. Guillemet-Fritsch, J. Therm. Anal. Calorim. 101 (2010) 137–142.
[23] E. Rios, P. Chartier, J.L. Gautier, Solid State Sci. 1 (1999) 267–277.
[24] F. Švegl, B. Orel, I. Grabec-Švegl, V. Kaučič, Electrochim. Acta 45 (2000) 4359–4371.
[25] H. Bordeneuve, S. Guillemet-Fritsch, A. Rousset, S. Schuurman, V. Poulain, J. Solid State Chem. 182 (2009) 396–401.
[26] Y.T. Jang, H.F. Wang, Y.M. Chiang, J. Mater. Chem. 8 (1998) 2761–2764.
[27] D.G. Wickham, W.J. Croft, J. Phys. Chem. Solids 7 (1958) 351–360.
[28] S. Naka, M. Inagaki, T. Tanaka, J. Mater. Sci. 7 (1972) 441–444.
[29] N. Bahlawane, Appl. Catal. B: Environ. 67 (2006) 168–176.
[30] N. Bahlawane, P.A. Premkumar, J. Feldmann, K. Kohse-Höinghaus, Chem. Vap. Deposition 12 (2007) 118–122.
[31] N. Bahlawane, P.H. Tchoua Ngamou, K. Kohse-Höinghaus, ECS Trans. 25 (2009) 265–272.
[32] Z.Y. Tian, N. Bahlawane, F. Qi, K. Kohse-Höinghaus, Catal. Commun. 11 (2009) 118–122.
[33] N. Bahlawane, P.H. Tchoua Ngamou, K. Kohse-Höinghaus, J. Electrochem. Soc. 157 (2010) D16–D20.
[34] P.H. Tchoua Ngamou, N. Bahlawane, J. Solid State Chem. 182 (2009) 849–854.
[35] P.H. Tchoua Ngamou, N. Bahlawane, Chem. Mater. 22 (2010) 4158–4165.
[36] P.H. Tchoua Ngamou, K. Kohse-Höinghaus, N. Bahlawane, Catal. Commun. 12 (2011) 1344–1350.
[37] N. Bahlawane, P.H. Tchoua Ngamou, V. Vannier, T. Kottke, J. Heberle, K. Kohse-Höinghaus, Phys. Chem. Chem. Phys. 11 (2009) 9224–9232.
[38] N. Bahlawane, P.A. Premkumar, Z.Y. Tian, X. Hong, F. Qi, K. Kohse-Hoinghaus, Chem. Mater. 22 (2010) 92–100.
[39] Y.Z. Jiang, N. Bahlawane, J. Phys. Chem. C 114 (2010) 5121–5125.
[40] V. Vannier, M. Schenk, K. Kohse-Höinghaus, N. Bahlawane, J. Mater. Sci. 47 (2012) 1348–1353.

[41] A. Askarinejad, A. Morsali, Ultrason. Sonochem. 16 (2009) 124–131.
[42] V.G. Hadjiev, M.N. Iliev, I.V. Vergilov, J. Phys C: Solid State Phys. 21 (1988) L199–L201.
[43] F. Gu, C.Z. Li, Y.J. Hu, L. Zhang, J. Cryst. Growth 304 (2007) 369–373.
[44] C.F. Windisch, G.J. Exarhos, K.F. Ferris, M.H. Engelhard, D.C. Stewart, Thin Solid Films 398 (2001) 45–52.
[45] C.M. Julien, M. Massot, J. Phys. Condens. Matter 15 (2003) 3151–3162.
[46] B. Ammundsen, G.R. Burns, M.S. Islam, H. Kanoh, J. Rozière, J. Phys. Chem. B 103 (1999) 5175–5180.
[47] L. Malavasi, P. Galinettob, M.C. Mozzatib, C.B. Azzoni, G. Flor, Phys. Chem. Chem. Phys. 4 (2002) 3876–3880.
[48] M. Kim, X.M. Chen, E. Fradkin, P. Abbamonte, S.L. Cooper, Phys. Rev. Lett. 105 (2010) 026402.
[49] R.D. Shannon, Acta Crystallogr. A 32 (1976) 751–767.
[50] D. Barreca, C. Massignan, S. Daolio, M. Fabrizio, C. Piccirillo, L. Armealo, E. Tondello, Chem. Mater. 13 (2001) 588–593.
[51] S. Todorova, H. Kolev, J.P. Holgado, G. Kadinov, C. Bonev, R. Pereniguez, A. Caballero, Appl. Catal. B: Environ. 94 (2010) 46–54.
[52] J.L. Gautier, C. Cabezas, J. Electroanal. Chem. 159 (1983) 137–153.
[53] S. Valeri, A. Borghi, G.C. Gazzadi, A. Dibona, Surf. Sci. 423 (1999) 346–356.
[54] S.G. Christoskova, M. Stoyanova, M. Georgieva, D. Mehandjiev, Mater. Chem. Phys. 60 (1999) 39–43.
[55] Q.H. Zhang, X.H. Liu, W.Q. Fan, Y. Wang, Appl. Catal. B: Environ. 102 (2011) 207–214.
[56] D.G. Klissurski, E.L. Uzunova, Appl. Surf. Sci. 214 (2003) 370–374.
[57] J. Feldmann, N. Bahlawane, K. Kohse-Höinghaus, Elecrochem Proceedings of EUROCVD-15, The Electrochemical Society, 2005–09, 2005, pp. 659–666.
[58] F. Wyrwalski, J.-M. Glraudon, J.-F. Lamonier, Catal. Lett. 137 (2010) 141–149.
[59] E.J.W. Verwey, Semiconducting Materials, Butterworths Scientific Publications, London, 1951.
[60] S. Ivanova, C. Petit, V. Pitchon, Gold Bull. 39 (2006) 3–8.
[61] H. Noller, H. Vinek, J. Mol. Catal. 51 (1989) 285–294.